Original Research Article

Mathematical approach to design 3D scaffolds for the 3D printable bone implant

Wiktoria Wojnicz [a,*], **Marek Augustyniak** [b], **Piotr Borzyszkowski** [b]

[a] Faculty of Mechanical Engineering and Ship Technology, Gdansk University of Technology, Gdansk, Poland
[b] Faculty of Applied Physics and Mathematics, Gdansk University of Technology, Gdansk, Poland

ARTICLE INFO

ABSTRACT

This work demonstrates that an artificial scaffold structure can be designed to exhibit mechanical properties close to the ones of real bone tissue, thus highly reducing the stress-shielding phenomenon. In this study the scan of lumbar vertebra fragment was reproduced to create a numerical 3D model (this model was called the reference bone sample). New nine 3D scaffold samples were designed and their numerical models were created. Using the finite element analysis, a static compression test was performed to assess the effective Young modulus of each tested sample. Also, two important metrics of each sample were assessed: relative density and surface area. Each new designed 3D scaffold sample was analyzed by considering two types of material properties: metal alloy properties (Ti-6Al-4V) and ABS polymer properties. Numerical analysis results of this study confirm that 3D scaffold used to design a periodic structure, either based on interconnected beams (A, B, C, D, E and F units) or made by removing regular shapes from base solid cubes (G, H, I units), can be refined to obtain mechanical properties similar to the ones of trabecular bone tissue. Experimental validation was performed on seven scaffolds (A, B, C, D, E, F and H units) printed from ABS material without any support materials by using Fused Deposition Modeling (FMD) technology. Results of experimental Young modulus of each printed scaffold are also presented and discussed.

1. Introduction

Using a biocompatible artificial material to fill the bone loss requires solving of several engineering problems. In particular, mechanical properties of the implant should be similar to the ones of the real bone tissue, firstly to assure the demanded carrying capacity of the whole bone after reconstruction, secondly to avoid stress-shielding phenomenon that leads to the local weakening/strengthening and causes bone resorption (bone loss), aseptic loosening and/or develop-

ment of osteoporosis [1–8]. Moreover, an implant should have a high fatigue resistance and crack-development resistance. Also, biocompatibility of the implant is essential requirement since it allows connecting the bone tissue with implant and inducing osseointegration and bone tissue regeneration process [1,6,9–11].

Stiffness and strength of the implant are dependent on several factors: 1) chemical constitution of the implant material; 2) micro/meso-structure of the implant; 3) mechanical properties of bone fragments used to fix this implant; 4) method of implant fixation to the bone fragments; 4) configuration of implant and bone fragment system and load distribution. It is worth mentioning that in practice the third factor is very hard to assess due to stochastic porosity, complex geometry and non-linear mechanical properties of the bone tissue. That is why to identify these features and properties sophisticated tools should be used. Numerical methods are helpful in analyzing biomechanical problems and generating new solutions in medicine and veterinary sciences [12]. For example, it was possible to create a finite element model (FE model) of the implant [5,6] or the trabecular bone sample or a cortical one [6,13]. The patient-specific reconstruction of tissues is performed in practice thanks to the advent of both commercial (Mimics, SliceOMatic, OsiriX) and freeware (Snap-ITK) computer software.

To avoid problem of stress shielding the patient-specific implant should be light-weight and high-strength structure. A lattice material (lattice structure) meets these requirements and also can absorb impact loading [14]. A lattice material is composed of spatial scaffolds that are designed by considering structural, dimensional, stiffness and/or strength requirements [2,15–19]. To meet these requirements different optimization approaches are applied, i.e. topological optimization methods [19,21], multiscale topology optimization to design optimal lattice structure to maximize the structure stiffness [20]. However, the challenge is to create a lattice structure that has mechanical properties similar to the ones of the real bone tissue and produce this structure by considering limitations of 3D printing technology.

As far as the constitutive material of the bone implant is concerned, there is wide range of available biocompatible materials including photopolymer resins, ceramic paste, temperature sensitive polymers, thermoplastics (PCL, PLA, ABS), metal foil, metal powder, and ceramic powder [22]. Before choosing a suitable material, its possibility to manufacture by proper Additive Manufacturing technics must be considered. For example, ceramic and metal powders are suitable for selective laser sintering or melting technique (SLS/SLM), electron beam melting (EBM), or direct metal deposition (DMD). For polymers in form of solidifiable fluid, the stereolitography (SLA) or microextrusion are most suitable techniques, and for elastic filaments like ABS or PLA, the best technique is fused deposition modeling (FDM). One of the most widely used metals for bone implants is titanium alloy Ti-6Al-4V [23]. In the paper [24] the authors proposed this alloy for scaffolds for large, segmental defects of bone, and implanted the graft into a 30-mm segmental defect of goat metatarsus. Their scaffolds were manufactured by EBM with different pore sizes and they obtained structures with Young modulus within the range 1.7–3.7 GPa.

Another widely used material for FDM method is thermoplastic ABS [18,25]. It is amorphous polymer that is available in a form of flexible filament for 3D printing. Comparing it to other thermoplastics, ABS has good toughness and impact resistance, and these properties can vary with its chemical composition. Besides, there are available variations of ABS, which exhibit good biocompatibility.

Mechanical properties of designed scaffolds can be assessed by performing mechanical tests, i.e. static compression test (to assess Young modulus and yield strength) [7,21,25,26], flexural test (bending test) [27,28]. Designing a test, one should consider a scaffold porosity that has a big impact on the mechanical properties of the tested scaffold [8,10,26,29,30].

The structure of bone tissue may vary in porosity, depending on the type of bone, depth from the surface, patient age, stage of osteoporosis etc. The difference between the Young modulus of the bone tissue and the one of the implant may induce a stress shielding phenomenon. To avoid this one has to design an implant which mechanical properties should be similar to the ones of the bone fragments used to fix this implant and carry the load. **The main motivation** of this study was to create a new mathematical approach to design numerical models of 3D scaffold structures that can be used to produce 3D printable bone implants to reconstruct trabecular bone tissue deficiencies. **The aim of the study** was to design numerical models of spatial scaffold structures (lattice materials) for the 3D printable bone implants. **The scope of this study** involved numerical research by using FE method and experimental validation of proposed scaffolds produced by using a Fused Deposition Modeling (FMD) technology. The 3D numerical model of the human trabecular bone fragment were created and treated as a reference bone model. New nine 3D scaffold samples were designed and their numerical models were tested. Numerical research were conducted to assess physical properties of model of the reference bone sample and nine designed 3D scaffold samples.

2.   Materials and methods

2.1.   Numerical model of the reference bone sample

The micro-Computed Tomography (µCT) scan of the lumbar vertebra of anonymous patient was received in the form of 159 slices from the Marian Smoluchowski Institute of Physics (Declaration of Ethics Committee Approval of Marian Smoluchowski Institute of Physics, 13.01.2020). Scan was firstly converted into DICOM file, and then converted into the STL format by using ITK-Snap software. To create a numerical 3D model the HyperMesh software was used. This model was called the reference bone sample (Fig. 1) and it was composed of 189 024 nodes and 780 924 linear tetrahedral solid elements (average element size: 0.05 mm). A relative density of this reference bone sample was assessed as the ratio of its volume (bulk of material) and the volume of cylinder enclosing this porous structure [30]. Obtained relative density of this sample was equal to 13.21%.

To determine a Young modulus of the reference bone sample a static compression numerical test was conducted by

Fig. 1 – Numerical 3D model of lumbar vertebra fragment (reference bone sample).

using OptiStruct software. This analysis was performed in a linear elastic range by setting material properties of the 3D model according to [31]: Young modulus was set to 20 GPa and Poisson's ratio was set to 0.3. A static compression test was implemented according to the following setup. This test was conducted in a linear-elastic range of material behaviour by avoiding any numerical buckling phenomena [32]. The axial force 10 N acted along the Z axis of the global coordinate system through the rigid disc (this Z axis was a vertical axis in Fig. 2A). This disc was connected with the top surface of the model via penalty frictionless type contact (node-to-surface) to assure the homogeneous distribution of this axial force load. Boundary conditions were formulated as follows (Fig. 2A). The constraints were applied to all nodes of the model bottom base. One node placed in the middle of bottom base was constrained in all translational directions (along the X-axis, Y-axis and Z-axis). All other nodes of this bottom base were constrained in one translational direction along the Z-axis. This setup of boundary conditions and force application was adopted to test all designed 3D scaffold samples (p. 2.3). The effective Young modulus E was assessed according to the Hooke's law [4,11]:

$$E = \frac{F \cdot l_0}{\Delta l \cdot A}$$

where: F – axial force, A – surface area of the sample, Δl – average vertical displacement of the model [23], l – original height of the sample.

The effective Young modulus of the reference bone sample obtained by performing static compression test was equal to 0.35 GPa. This value is consistent with published ones [0.09; 0.5] GPa [33,34].
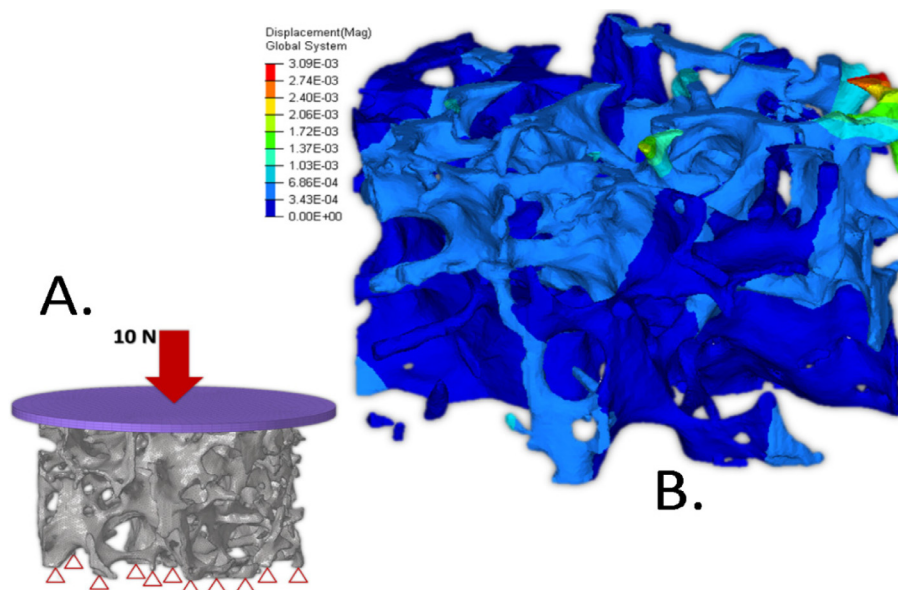

Fig. 2 – A) Numerical model of the reference bone sample in static compression numerical test; B) chosen results of vertical displacements.

2.2.   Design of 3D scaffold units

To design a fragment of trabecular bone one can consider different types of scaffold structure by modifying the pore size, surface area and dimensions of base unit. In the scope of this study nine new 3D scaffold units were created and their finite element models were generated (Fig. 3). The unit A is based on a regular cubic structure. The unit B is based on the face centered cubic structure (FCC). The unit C is created on the body centered cubic topology (BCC). The unit D is based on the truncated octahedron topology. The unit E is based on the octahedron topology. The unit F is a rhombic dodecahedron structure. Each of these six units (A, B, C, D, E and F) was composed of the solid beams connected according to the given topology. The last three units (G, H, and I) were designed by material subtraction from the base solid cubes (Figs. 3–4). In particular, the unit G was created by removing from the base cube three perpendicular cylinders. The unit
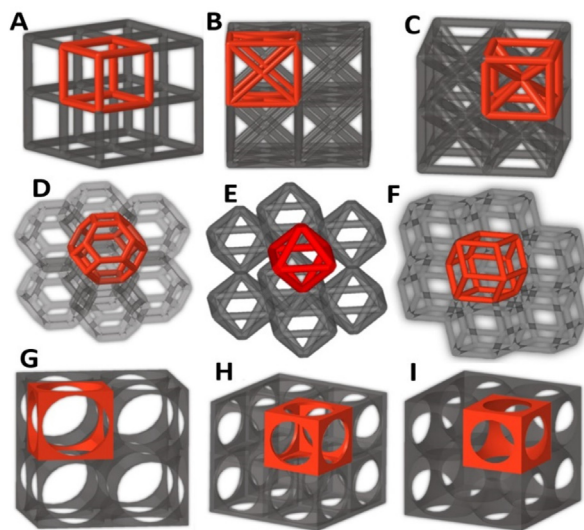

Fig. 3 – New designed 3D scaffold units. A – regular cubic structure (A unit); B – FCC structure (B unit); C – BCC structure (C unit); D – truncated octahedron structure (D unit); E – octahedron structure (E unit); F – rhombic dodecahedron structure (F unit); G, H, I – subtractive structures (G unit, H unit and I unit, respectively).

H was designed by removing from the base cube a smaller cube placed in the centre and three perpendicular cylinders. The unit I was created by hollowing a base cube with a sphere of higher diameter than cube's edge (a sphere was placed at the center of intersection of base cube diagonals). In this work, the thickness of "wall" of the unit H was assumed to be constant. The distance between pores in two adjacent unit cells was called effective thickness (te).

2.3.   Design of 3D scaffold samples

Steps of building of **3D scaffold samples** are shown in Fig. 5. First, a certain topology of unit is chosen (p.2.2) and a single 3D scaffold unit is created (step 1–2). Next, a 3D scaffold sample (lattice material) is built by multiplying the 3D scaffold units and merging them at the common surfaces (step 3). After that, a cylindrical sample (3 mm height and 5 mm base diameter) is extracted by using Boolean solid operations (step 4). The resulting geometry of cylindrical sample is finally meshed with linear tetrahedral solid elements of average size equal 0.05 mm (half of the assumed typical manufacturability limit).

In order to obtain a relative density of each cylindrical sample, two geometrical models were produced. The first one is a solid representation of this cylindrical sample. The second model has the internal structure of the tested unit and external shape cut by using Boolean operations (Fig. 6). A relative density is calculated as a ratio of the second model volume to the first model volume.

The active surface area of each sample (called surface area) was calculated by creating a temporary 2D mesh juxtaposed with the 3D mesh of the model and summing up areas of all internal surfaces. All calculations were conducted in a preprocessor of HyperMesh sotware.

The algorithm of determination of parameters of new designed 3D scaffold units and samples is summarized in Table 1. This algorithm has four steps. At each stage one parameter (called variable) was manually tuned to achieve a given objective.

2.4.   Testing 3D scaffold samples

To assess the effective Young modulus of each new designed 3D scaffold sample, a numerical static compression test was performed in linear-elastic range of material behaviour according to the rules described in p.2.1. Each new designed
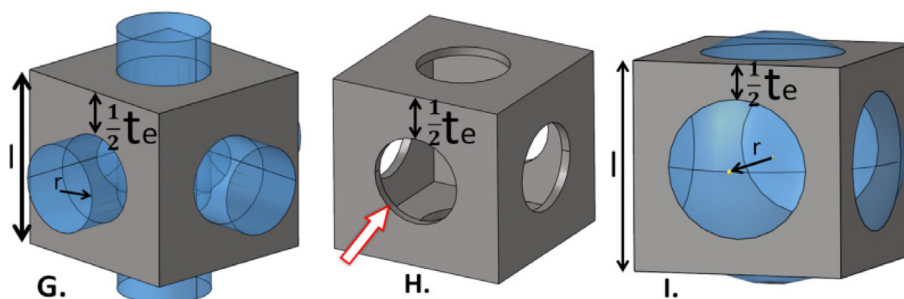
Fig. 4 – Specific dimensions of G, H and I units: l – unit's length, *te* – effective thickness, *r* – radius.
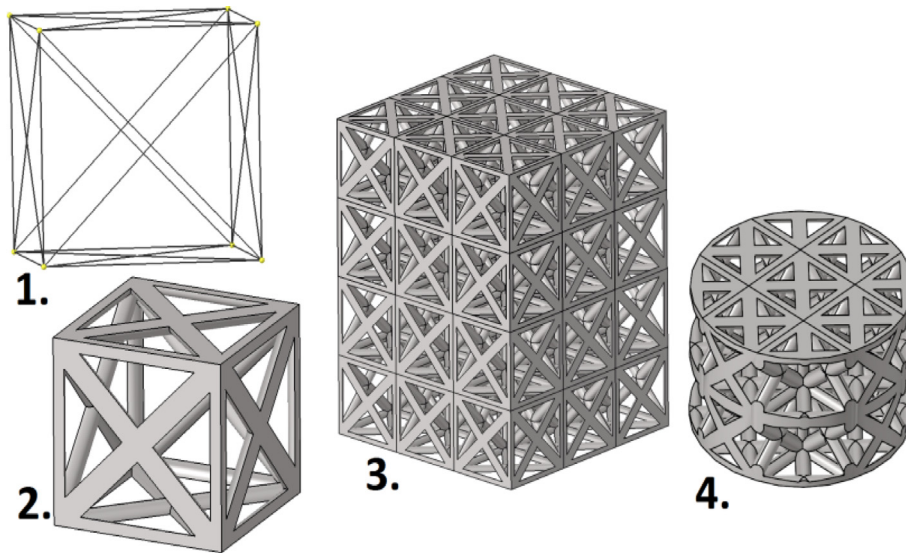
Fig. 5 – Visualisation of steps to design a new 3D scaffold structure.
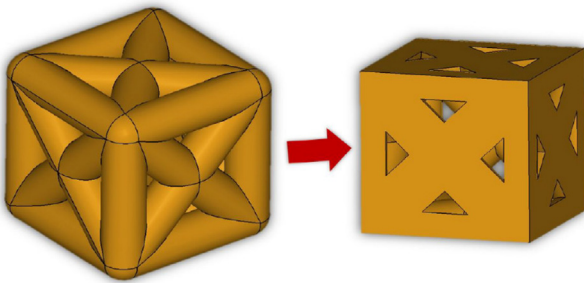

Fig. 6 – Visualisation of Boolean operations on a single B unit performed to calculate its relative density.

3D scaffold sample was analyzed by considering two types of material properties: 1) metal alloy properties (Ti-6Al-4V) with E = 110 GPa and Poisson's ratio equalled 0.35 [35–38]; 2) ABS polymer properties with E = 2 GPa and Poisson's ratio equalled 0.35 [18,25].

2.5. Validation

Experimental validation was carried out on the proposed 3D scaffold samples printed by using a FMD technology and acrylonitrile butadiene styrene material (ABS). Samples were printed by using Zortrax M200 printer (0.4 mm nozzle diameter, 0.14 mm layer thickness, 100% solid fitting). Due to the technical limitations of this printer it was not possible to print scaffolds with original lengths that were used in FEM research. That is why the volume of each scaffold was increased six times without any supporting materials (because it was not possible to remove supports without damage the scaffold sample). It is worth noticing that this extension of volume was the minimum one that allowed us to print seven scaffold samples: A unit, B unit, C unit, D unit, E unit, F unit and H unit (Figs. 7–8).

Using this printer, it was not possible to print scaffold samples for two units (G unit and I unit) without supports. That is why these two 3D scaffold samples were not validated.

To assess experimental Young modulus of each 3D printed scaffold (A unit, B unit, C unit, D unit, E unit, F unit and H unit) three samples were printed and carried out on the testing machine Zwick LTM10/Z010TE (10 kN) by performing static compressive test. The test was conducted by setting 10 mm/min velocity and 10 mm displacement.

3. Results

The summary of metrics for the reference bone sample and new designed 3D scaffold samples obtained after stage 3 and 4 of FEM research are presented in Table 2. Intermediate results (after stage 1 and 2) are not shown.

Conducting static compressive tests, seven 3D scaffold samples were tested and force–displacement relationships are presented within 3 mm displacement: A unit (regular cubic structure) (Fig. 9A), B unit (FCC structure) (Fig. 9B), C unit (BCC structure) (Fig. 9C), D unit (truncated octahedron structure) (Fig. 9D), E unit (octahedron structure) (Fig. 9E), F unit (rhombic dodecahedron structure) (Fig. 9F), H unit (subtractive structure) (Fig. 9G).

Performing visual inspection of examined samples that were obtained for 10 mm displacement (Fig. 7 and Fig. 8), one can identify two types of fracture: 1) flattened samples without delamination (B unit, C unit, E unit and H unit) and flattened samples with delamination (A unit, D unit and F unit).

It is worth paying attention that experimental Young modulus for each printed 3D scaffold sample was assessed in the linear-elastic range of material behavior by assuming that normal stress in FEM research and experimental validation was the same. The results of experimental Young modulus are given as a mean ± SD (Table 3). Absolute relative errors were assessed by calculating difference between effective

Table 1 – Stages of determination of parameters of new designed 3D scaffold units and samples.

	Model extent	Fixed parameter	Variable(s)	Objective	Comments
1	Single unit	Unit size (1x1x1mm)	Beam diameter or wall thickness (A, B, C, D, E, F, G, H and I units)	Fitting to obtain a relative density of single unit close to the one of the reference bone unit	- Set of manufacturability constraints to obtain results with discrepancy no more than 0.1 mm - Discrepancies up to 15% due to the discrete stepping of dimensions
2	Single unit	Beam diameter or wall thickness taken from Stage 1	Unit size	Fitting to obtain a surface of single unit close to the one of the reference bone unit	
3	Cylindrical sample	Beam diameter or wall thickness taken from Stage 1 + Unit size taken from Stage 2	None	Assessment of effective Young modulus of cylindrical sample and recalculation its relative density and surface area	- No optimization - Relative density and surface areas only slightly affected by boundary effects
4	Cylindrical sample	Two "best" topologies (F and H units) + Unit size taken from Stage 2	Beam diameter (F unit) or wall thickness (H units)	Fitting to obtain the effective Young modulus of cylindrical sample close to the one of the reference bone sample	- Focusing on Young modulus fitting increases inevitable divergence between a relative density and surface area of the tuned sample and reference bone sample. Some trade-off has to be done

Young modulus and experimental Young modulus with respect to the effective Young modulus.

4. Discussion

Considering FEM results of effective Young moduli assessed for the samples composed of A, B, C, D, E, F, G, H and I units (Table 2), we found that values of Ti6Al4V samples are higher with respect to the ones of ABS samples. Analysing metallic material results, three samples have the highest values: I unit sample (6.08 GPa), H unit sample (5.87 GPa) and A unit sample (5.85 GPa). In a case of polymer results the highest values are found for H unit sample (0.19 GPa), I unit sample (0.18 GP) and A unit sample (0.17 GPa). Comparing these highest values with the effective Young modulus of the reference bone sample, we see that: 1) Ti6Al4V results are 17 times higher on average with respect to the result of reference bone sample; 2) ABS results are twice smaller on average with respect to the results of reference bone sample.

Aiming to retune beams diameters (A–F units) and wall thickness (G–I units) and to achieve the effective Young modulus close to the one of reference bone sample (0.35 GPa), two samples had been chosen: F unit sample and H unit sample. We created "F – optimized unit made of Ti-6Al-4V" and "H – optimized unit made of ABS" samples and after they both were refined on the stage 4 (Table 1). In both cases it was possible to obtain the value of the effective Young modulus very close to the one of the reference bone sample (0.33 GPa and 0.32 GPa, respectively).

In "F – optimized unit made of Ti-6Al-4 V" sample the radius of the beam was changed from 0.2 mm to 0.14 mm to obtain a given value of the effective Young modulus (see Fig. 10). However, this fitting caused some divergence in remaining metrics with respect to the reference bone sample metrics: this optimized unit made of Ti-6Al-4 V has smaller relative density (7.50% vs 13.21%) and surface area (2.05 mm^2 vs 2.78 mm^2).

To obtain a value of effective Young modulus close to the given one (reference bone sample) the "H – optimized unit made of ABS" sample was modified by increasing the wall thickness 0.12 mm to 0.24 mm (Fig. 11). With respect to the reference bone sample metrics, this new structure made of ABS has a bit bigger relative density (15.66% vs 13.21%) and surface area (2.85 mm^2 vs 2.78 mm^2)

Analyzing presented results obtained on the base of FEM analysis with published ones, some indirect comparison can be made by considering published reports related to the trabecular bone properties and scaffolds made of titanium or Ti-6Al-4 V. There is lack in evidence related to the scaffold made of ABS. Considering assessed value of effective Young modulus (0.35 GPa), we found that this value is in a good agreement with a result 0.155 GPa given in [4,5], 0.1–0.2 GPa reported in [26], minimum value 0.788 GPa reported in [39] and 0.76–18.2 GPa presented in [7].

Considering published data referred to the compressive testing of scaffolds made of titanium or Ti-6Al-4V, we can see that our data (FEM analysis) related to the new designed scaffolds made of Ti-6Al-4V (E = 0.33–6.08GPa) are in a good agreement with the results presented in [7,21].
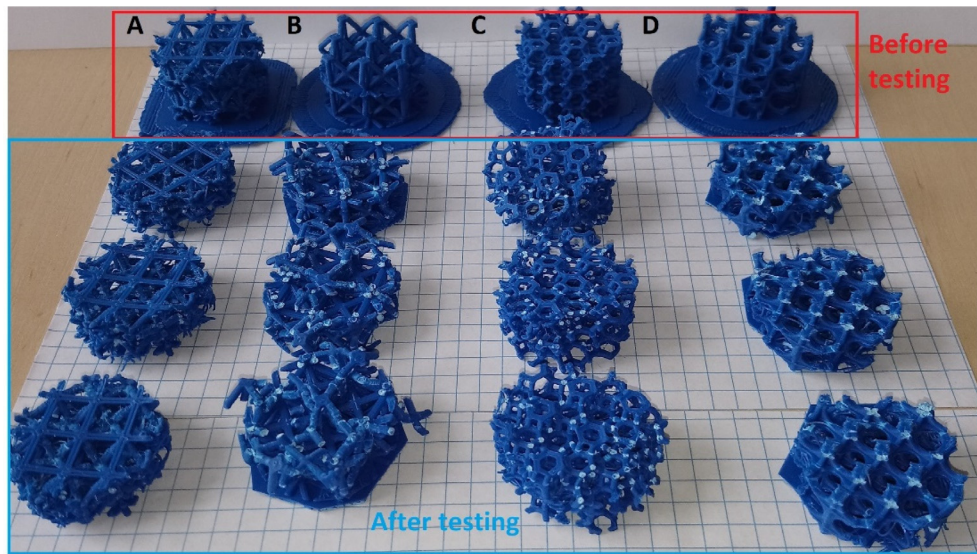
Fig. 7 – A) C unit (BCC structure); B) B unit (FCC structure); C) D unit (truncated octahedron structure); D) H unit (subtractive structure).
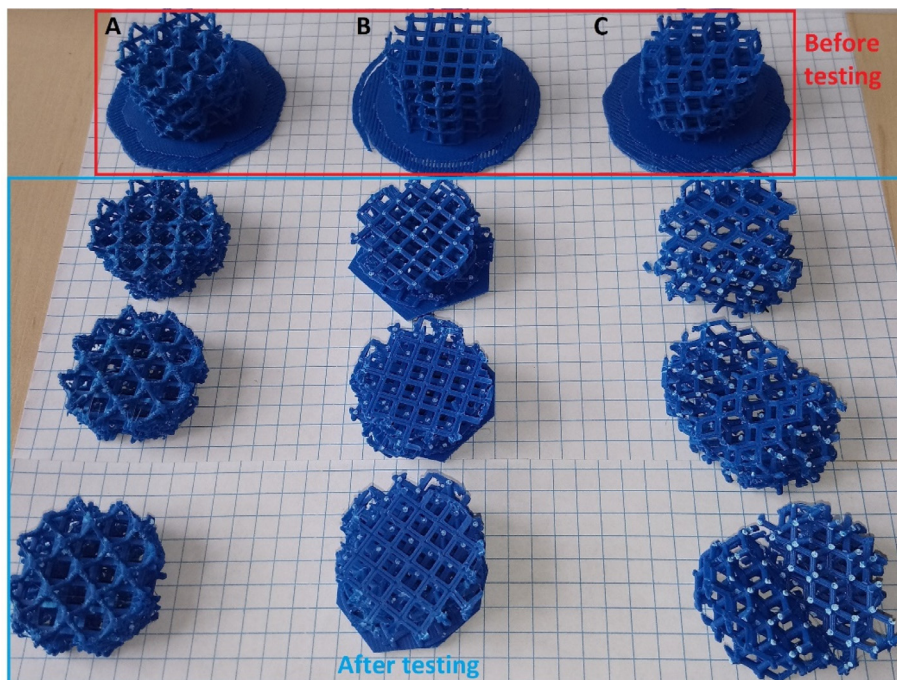

Fig. 8 – A) E unit (octahedron structure); B) A unit (regular cubic structure); C) F unit (rhombic dodecahedron structure).

The paper [7] reports the range of compressive Young modulus 1.05–12.01 GPa obtained from a testing of lattice titanium structures that were designed to target the range of trabecular bone Young modulus 0.76–18.2 GPa. Considering relative density in the interval (0; 1), the paper [21] reports two approximated ranges of Young modulus calculated for two types of Ti-6Al-4V scaffolds: (2; 20) GPa for Schwarz IWP lattice structure and (1; 10) GPa for Schoen Gyroid lattice structure. Moreover, [4,5] describes porous Ti-6Al-4V scaffold designed as diamond cubic lattice structure with hexagonal cross-sections strut and truncated tetrahedron nodes. The Authors declare that the Young modulus of this scaffold equals 8.4 GPa. The paper [8] reports results related to the Ti-6Al-4V (honeycomb, octahedral) scaffolds compressive testing in a form of graphical relations between normal force (N) and deformation (mm). On the base of these results one can assess coefficients of stiffness (N/mm) but there is lack of data needed to calculate Young modulus. That is why in this case it is hard to perform direct analysis.

Comparing results of effective Young modulus with the experimental ones, we found that: 1) the smallest relative error

Table 2 – FEM research summary of metrics of reference bone sample and new designed 3D scaffold samples.

Sample	Analysis Stage	Unit size [mm]	Relative density [%]	Surface area [mm^2]	E (Ti6-Al-4V) [GPa]	E (ABS) [GPa]
Reference bone unit	0	–	13.21	2.78	0.35	
A unit	3	0.84	12.44	2.85	5.85	0.17
B unit	3	1.77	15.35	2.85	4.64	0.14
C unit	3	1.45	14.56	2.78	2.91	0.09
D unit	3	1.04	13.73	2.89	1.61	0.05
E unit	3	0.79	11.07	2.87	1.66	0.05
F unit	3	1.12	14.04	2.85	1.57	0.05
G unit	3	1.10	12.53	2.00	3.56	0.10
H unit	3	1.10	13.99	2.84	5.87	0.19
I unit	3	0.82	11.12	2.85	6.08	0.18
F – optimized unit made of Ti-6Al-4V	4	1.12	7.50	2.05	0.33	–
H – optimized unit made of ABS	4	1.10	15.66	2.85	–	0.32
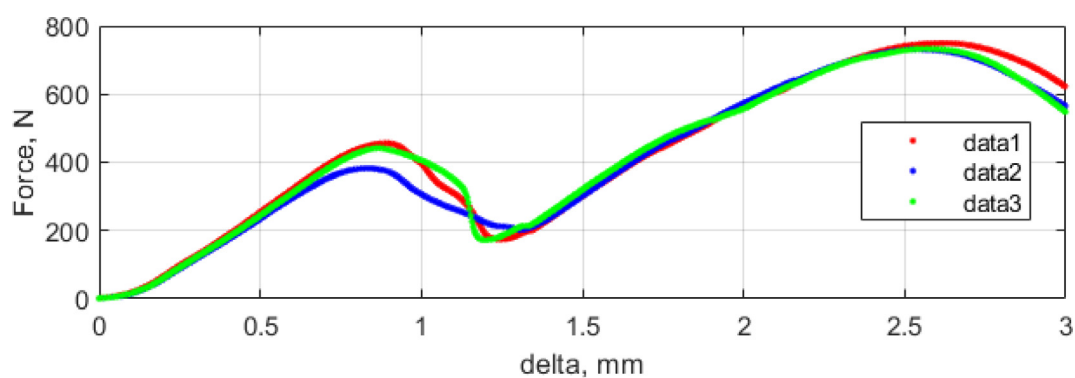
Fig. 9A – Force-displacement experimental relations of A unit (regular cubic structure).
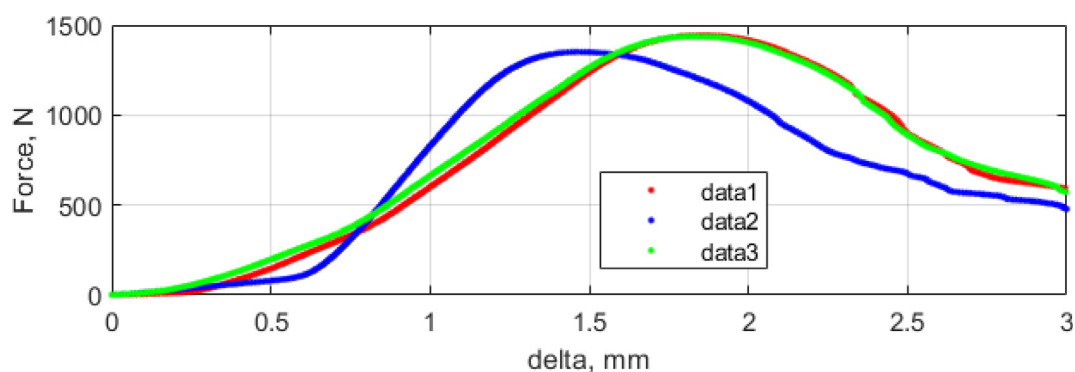
Fig. 9B – Force-displacement experimental relations of B unit (FCC structure).
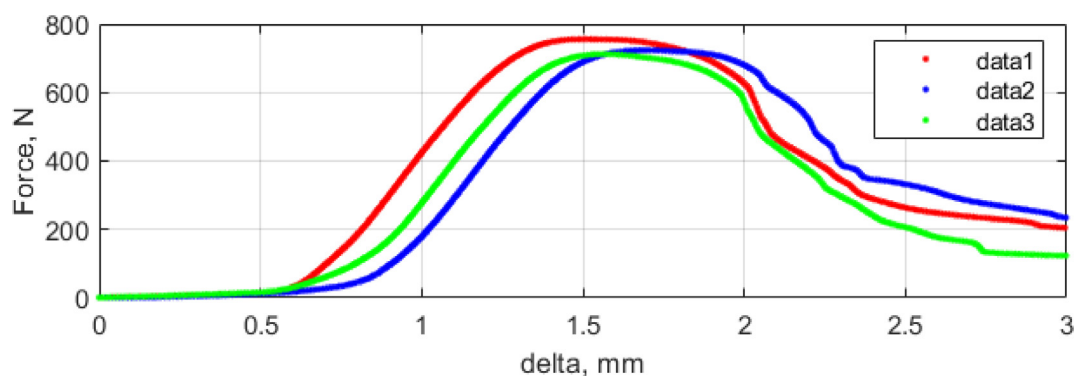
Fig. 9C – Force-displacement experimental relations of C unit (BCC structure).
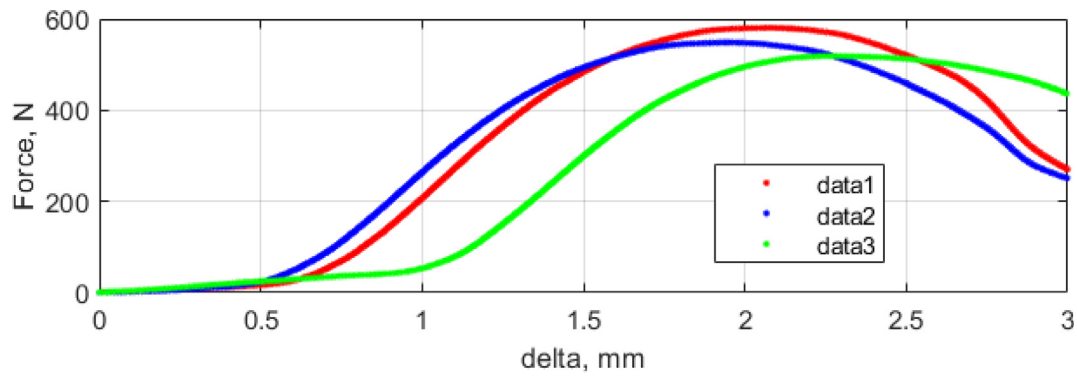
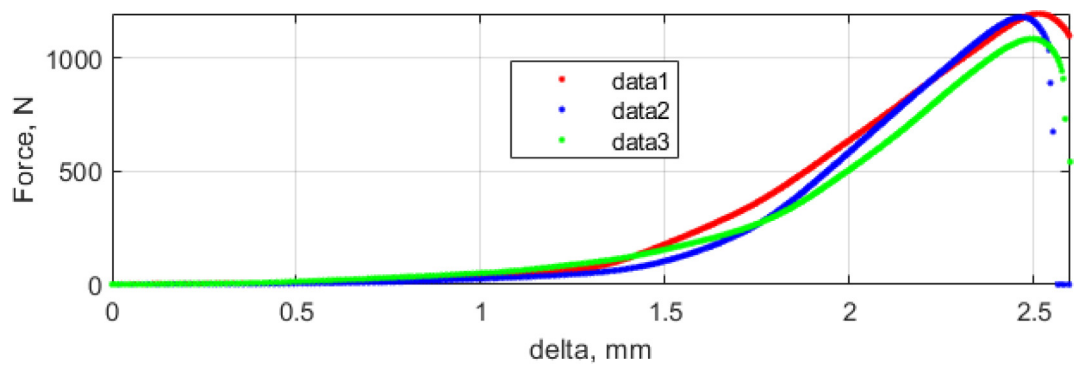**Fig. 9D – Force-displacement experimental relations of D unit (truncated octahedron structure).**

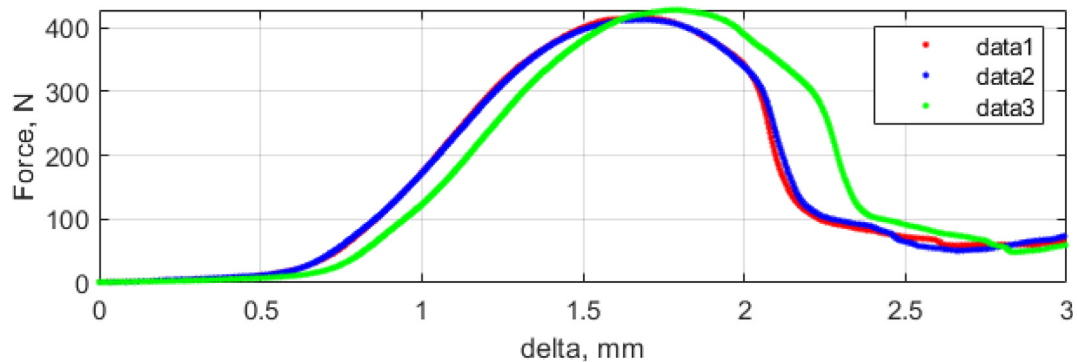**Fig. 9E – Force-displacement experimental relations of E unit (octahedron structure).**

Fig. 9F – Force-displacement experimental relations of F unit (rhombic dodecahedron structure).
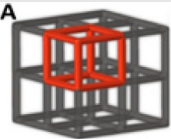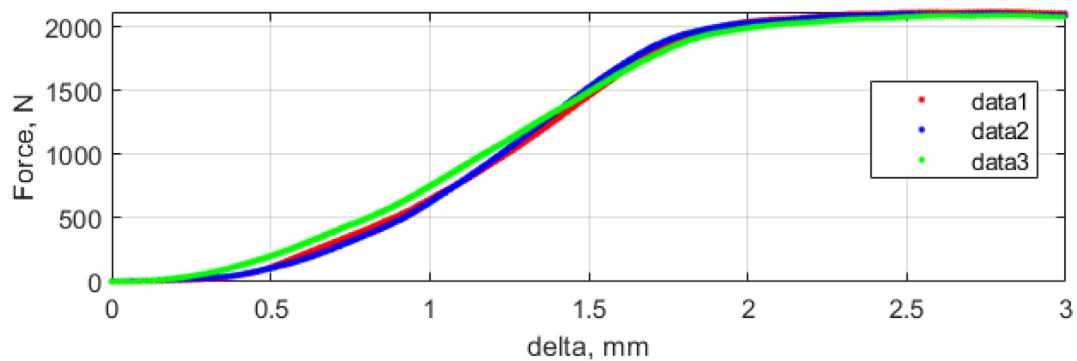

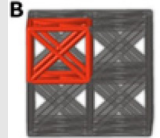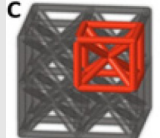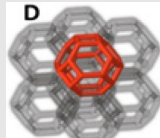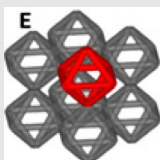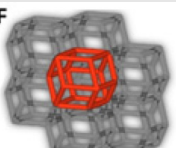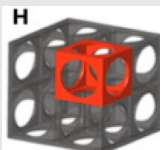**Fig. 9G – Force-displacement experimental relations of H unit (subtractive structure).**

Table 3 – Experimental Young modulus results

Unit	Experimental effective Young modulus [MPa]	Relative error [%]
	A unit (regular cubic structure) E = 117.6 ± 6.4 MPa	30.8%
	B unit (FCC structure) E = 101.8 ± 14.2 MPa	27.3%
	C unit (BCC structure) E = 75.6 ± 6.5 MPa	16.0%
	D unit (truncated octahedron structure) E = 60.8 ± 9.6 MPa	21.6%
	E unit (octahedron structure) E = 59.3 ± 3.3 MPa	18.6%
	F unit (rhombic dodecahedron structure) E = 52.3 ± 0.7 MPa	4.6%
	H unit (subtractive structure) E = 114.2 ± 9.6 MPa	40.0%

sample. Moreover, we performed experimental validations of seven new 3D scaffolds (A, B, C, D, E, F and H) produced from ABS material and printed without any support materials in FMD technology. Experimental Young modulus were assessed for these printed scaffolds by carrying out compressive tests on the testing machine. It is worth emphasizing that presented results are promising from the point of view of producing artificial bone tissue by using 3D printing to avoid stress-shielding phenomenon that can happen between stiff implant and soft bone tissue.
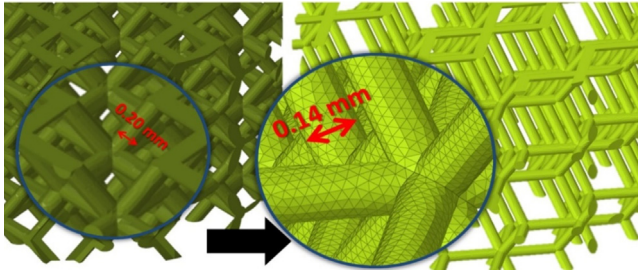
Fig. 10 – Visualisation of design of initial sample composed of F units (left) and sample of F optimized unit made of Ti-6Al-4V (right).
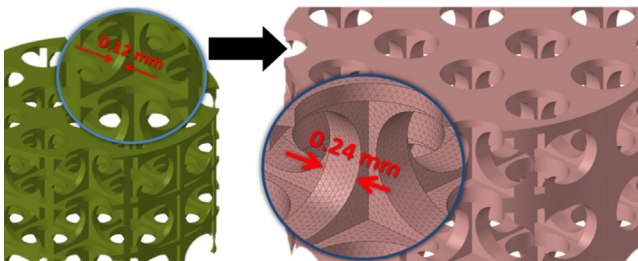

Fig. 11 – Visualisation of design of initial sample composed of H units (left) and sample of H optimized unit made of ABS (right).

It is worth paying attention that spatial configuration of the unit with respect to the applied load has a tremendous influence on the obtained results. We built new designed 3D scaffold samples by considering their initial configurations (Fig. 3). In future study different configurations have to be tested, especially paying attention to the configuration of the principal axes of the tested samples. Moreover, the following problems have to be tackled: 1) creating a model of trabecular bone tissue, the stress shielding phenomenon could be studied in "bone tissue – new 3D scaffold sample" system subjected to the external load by implementing a remodelling effect in bone tissue [7,10]; 2) implementation of some automatic optimization algorithm to design 3D complex scaffold (e.g. GA or gradient-based); 3) producing 3D prints samples of the selected structures, demonstrating their manufacturability and determining mechanical characteristics [40–42]; 4) extending the presented procedure to generate different bone tissue scaffolds and find the optimum synthetic bone structures (possibly irregular structure, non-homogeneous and anisotropic) [23,43,44].

Declaration of interest

The authors don't have any competing interests to declare.

The funding sources had not been involvement to conduct of this research.

CRediT authorship contribution statement

Wiktoria Wojnicz: Experimental validation, Data processing, Conceptualization, Methodology, Supervision, Writing - original

draft, Writing - review & editing. **Marek Augustyniak:** Conceptualization, Methodology, Project administration, Supervision, Writing - original draft. **Piotr Borzyszkowski:** Investigation, Methodology, Software, Visualization.

Acknowledgements

REFERENCES

[1] Bhuiyan DB, Middleton JC, Tannenbaum R, Wick TM. Mechanical properties and osteogenic potential of hydroxyapatite-PLGA-collagen biomaterial for bone regeneration. J Biomater Sci Polym Ed 2016;27(11):1139–54.

[2] Rho JY, Kuhn-Spearing L, Zioupos P. Mechanical properties and the hierarchical structure of bone. Med Eng Phys 1998;20:92–102.

[3] Ahmed K, Greene RJ, Aston W, Briggs T, Pendegrass C, Moazen M, et al. Experimental validation of an ITAP numerical model and the effect of implant stem stiffness on bone strain energy. Ann Biomed Eng 2020;48:1382–95.

[4] Jetté B, Brailovski V, Simoneau C, Dumas M, Terriault P. Development and in vitro validation of a simplified numerical model for the design of a biomimetic femoral stem. J Mech Behav Biomed Mater 2018;77:539–50.

[5] Jetté B, Brailovski V, Dumas M, Simoneau C, Terriault P. Femoral stem incorporating a diamond cubic lattice structure: design, manufacture and testing. J Mech Behav Biomed Mater 2018;77:58–72.

[6] Jia D, Li F, Zhang C, Liu K, Zhang Y. Design and simulation analysis of Lattice bone plate based on finite element method, Mech Adv Mater Struct 2019;1665759.

[7] Chen WM, Xie YM, Imbalzano G, Shen J, Xu S, Lee SJ, et al. Lattice Ti structures with low rigidity but compatible mechanical strength: design of implant materials for trabecular bone. Int J Precis Eng Manuf 2016;17:793–9.

[8] Jamshidinia M, Wang L, Tong W, Kovacevic R. The bio-compatible dental implant designed by using non-stochastic porosity produced by Electron Beam Melting® (EBM). J Mater Process Technol 2014;8:1728–39.

[9] von Wilmowsky C, Moest T, Nkenke E, Stelzle F, Schlegel KA. Implants in bone: part II. Research on implant osseointegration: material testing, mechanical testing, imaging and histoanalytical methods. Oral Maxillofac Surg 2014;18(4):355–72.

[10] Mahmoud D, Elbestawi MA. Lattice structures and functionally graded materials applications in Additive Manufacturing of orthopedic implants: a Review. J Manuf Mater Process 2017;1(2):13.

[11] Zhou Z, Buchanan F, Mitchell C, Dunne N. Printability of calcium phosphate: calcium sulfate powders for the application of tissue engineered bone scaffolds using the 3D printing technique. Mater Sci Eng C Mater Biol Appl 2014;1 (38):1–10.

[12] Méhes E, Biri-Kovács B, Isai DG, Gulyás M, Nyitray L, Czirók A. Matrigel patterning reflects multicellular contractility. PLoS Comput Biol 2019;25(15) e1007431.

[13] Kadir MRA, Syahrom A, Ochsner A. Finite element analysis of idealised unit cell cancellous structure based on morphological indices of cancellous bone. Med Biol Eng Comput 2010;48:497–505.

[14] Doblare M, Garcia JM, Gomez MJ. Modelling bone tissue fracture a healing: a review. Eng Fract Mech 2004;71:1809–40.

[15] Yoo D. New paradigms in internal architecture design and freeform fabrication of tissue engineering porous scaffolds. Med Eng Phys 2012;32:762–76.

[16] Yang N, Gao L, Zhou K. Simple method to generate and fabricate stochastic porous scaffolds. Mater Sci Eng 2015;56:444–50.

[17] Yang N, Tian Y, Zhang D. Novel real function based method to construct heterogeneous porous scaffolds and additive manufacturing for use in medical engineering. Med Eng Phys 2015;37:1037–46.

[18] Pan C, Han Y, Ku J. Design and optimization of lattice structures: a review. Appl Sci 2020;10:6374.

[19] Panesar A, Abdi M, Hickman D, Ashcroft I. Strategies for functionally graded lattice structures derived using topology optimisation for Additive Manufacturing. Addit Manuf 2018;19:81–94.

[20] Hoang VN, Tran P, Vu VT, Nguyen-Xuan H. Design of lattice structures with direct multiscale topology optimization. Compos Struct 2020;252 112718.

[21] Barba D, Reed RC, Alabort E. Design of metallic lattices for bone implants by additive manufacturing. In: The Minerals, Metals & Materials Society (eds) TMS 2020 149th Annual Meeting & Exhibition Supplemental Proceedings. The Minerals, Metals & Materials Series. Springer, Cham. 2020:745-759.

[22] Vastola G, Zhang G, Pei QX, Zhang YW. Modeling the microstructure evolution during additive manufacturing of Ti6Al4V: a comparison between electron beam melting and selective laser melting. JOM 2016;68:1370–5.

[23] Wieding J, Souffrant R, Mittermeier W, Bader R. Finite element analysis on the biomechanical stability of open porous titanium scaffolds for large segmental bone defects under physiological load conditions. Med Eng Phys 2013;35:422–32.

[24] Li G, Wang L, Pan W, Yang F, Jiang W, Wu X, et al. In vitro and in vivo study of additive manufactured porous Ti6Al4V scaffolds for repairing bone defects. Sci Rep 2016;6(1):34075.

[25] de la Lastra AA, Hixon KR, Aryan L, Banks AN, Lin AY, Hall AF, et al. Tissue engineering scaffolds fabricated in dissolvable 3D-printed molds for patient-specific craniofacial bone regeneration. J Funct Biomater 2018;9(3):46.

[26] Boga JC, Miguel SP, de Melo-Diogo D, Mendonça AG, Louro RO, Correia IJ. In vitro characterization of 3D printed scaffolds aimed at bone tissue regeneration. Colloids Surf BBiointerfaces 2018;165(1):207–18.

[27] Inzana JA, Olvera D, Fuller SM, Kelly JP, Graeve OA, Schwarz EM, et al. 3D printing of composite calcium phosphate and collagen scaffolds for bone regeneration. Biomaterials 2014;35(13):4026–34.

[28] Boehm AV, Meininger S, Tesch A, Gbureck U, Müller FA. The mechanical properties of biocompatible apatite bone cement reinforced with chemically activated carbon fibers. Materials (Basel) 2018;26(11):192.

[29] Nazir A, Abate KM, Kumar A, et al. A state-of-the-art review on types, design, optimization, and additive manufacturing of cellular structures. Int J Adv Manuf Technol 2019;104:3489–510.

[30] Moiduddin K, Al-Ahmari A, Al Kindi M, Nasr ESA, Mohammad A, Ramalingam M. Customized porous implants by additive manufacturing for zygomatic reconstruction. Biocybernetics Biomed Eng 2016;36:719–30.

[31] Podshivalov L, Gomes CM, Zocca A, Guenster J, Bar-Yoseph P, Fischer A. Design, analysis and additive manufacturing of porous structures for biocompatible micro-scale scaffolds. Procedia CIRP 2013;5:247–52.

[32] Nazir A, Jeng JW. Buckling behavior of additively manufactured cellular columns: Experimental and simulation validation. Mater Des 2020;186 108349.

[33] Oftadeh R, Perez-Viloria M, Villa-Camacho JC, Vaziri A, Nazarian A. Biomechanics and mechanobiology of trabecular bone: a review. J Biomech Eng 2015;137(1):0108021–01080215.

[34] Thavornyutikarn B, Chantarapanich N, Sitthiseripratip K, Thouas GA, Chen Q. Bone tissue engineering scaffolding: computer-aided scaffolding techniques. Prog Biomater 2014;3:61–102.

[35] Yánez A, Herrera A, Martel O, Monopoli D, Afonso H. Compressive behavior of gyroid lattice structures for human cancellous bone implant applications. Mater Sci Eng 2016;68:445–8.

[36] Feng Q, Tang Q, Liu Y, Setchi R, Soe S, Ma S, et al. Quasi-static analysis of mechanical properties of ti6al4v lattice structures manufactured using selective laser melting. Int J Adv Manuf Technol 2018;94:2301–13.

[37] Ra HK, Karthik NV, Gong H, Starr TL, Stucker BE. Microstructures and mechanical properties of ti6al4v parts fabricated by selective laser melting and electron beam melting. J Mater Eng Perform 2013;22:3872–83.

[38] Huynh V, Ngo NK, Golden TD. Surface activation and pretreatments for biocompatible metals and alloys used in biomedical applications, Review. Int J Biomater 2019 3806504.

[39] Cyganik Ł, Binkowski M, Kokot G, Rusin T, Popik P, Bolechała F, et al. Prediction of Young's modulus of trabeculae in microscale using macro-scale's relationships between bone density and mechanical properties. J Mech Behav Biomed Mater 2014;36:120–34.

[40] Egan PF, Gonella VC, Engensperger M, Ferguson SJ, Shea K. Computationally designed lattices with tuned properties for tissue engineering using 3D printing. PLoS One 2017;12(8) e0182902.

[41] Bandyopadhyay A, Dewangan VK, Vajanthri KY, Poddar S, Mahto SK. Easy and affordable method for rapid prototyping of tissue models in vitro using three-dimensional bioprinting. Biocybernetics Biomed Eng 2018;38:158–69.

[42] Szymczyk-Ziólkowska P, Labowska MB, Detyna J, Michalak I, Gruber P. A review of fabrication polymer scaffolds for biomedical applications using additive manufacturing techniques. Biocybernetics Biomed Eng 2020;40:624–38.

[43] Wojnicz W, Wittbrodt E. FEM approach to modeling of an irregular trabecular structure. Shell Structure: Theory and Applications.Vol.4. 1st ed., CRC Press/Balkema;2018, 519-522.

[44] Khan SN, Warkhedkar RM, Shyam AK. Analysis of Hounsfield unit of human bones for strength evaluation. Procedia Mater Sci 2014;6:512–9.